JGR Space Physics

RESEARCH ARTICLE
10.1029/2020JA028201

# An FDTD Investigation of Orthogonality and the Backscattering of HF Waves in the Presence of Ionospheric Irregularities

**D. R. Smith[1], T. Tan[2], E. Dao[3], C. Huang[3], and J. J. Simpson[1]**

[1]ECE Department, University of Utah, Salt Lake City, UT, USA, [2]ECE Department, Duke University, Durham, NC, USA, [3]Geospace Environment Impacts and Applications Branch, Air Force Research Laboratory, Kirtland, AFB, NM, USA

**Key Points:**

- The finite-difference time-domain model simulated high-frequency electromagnetic waves to interact with small ionospheric irregularities
- Lower-frequency waves propagating at high-elevation angles are seen to reach orthogonality in the presence of ionospheric irregularities
- Orthogonality is observed across a wide horizontal range of the ionosphere, and irregularities cause orthogonality to be reached abruptly

**Correspondence to:**
D. R. Smith,
dallinsmith9@gmail.com

**Citation:**
Smith, D. R., Tan, T., Dao, E., Huang, C., & Simpson, J. J. (2020). An FDTD investigation of orthogonality and the backscattering of HF waves in the presence of ionospheric irregularities. *Journal of Geophysical Research: Space Physics*, *125*, e2020JA028201. https://doi.org/10.1029/2020JA028201

Received 5 MAY 2020
Accepted 24 AUG 2020
Accepted article online 26 AUG 2020

**Abstract** One of the most successful instruments used to investigate the Earth's ionosphere is coherent scatter radars such as the Super Dual Auroral Radar Network (SuperDARN). Their method of mapping plasma convection at high latitudes is contingent on irregularities that momentarily exist in the ionosphere and are elongated along the direction of the geomagnetic field. Under these conditions, SuperDARN transmits high-frequency (HF) waves that are then backscattered from these plasma irregularities. In order for maximum backscatter to occur, the wave vector of the incident wave must be orthogonal to the magnetic field lines. This is called the "orthogonality condition." Over the years, ray tracing results have generated many assumptions, where and how orthogonality occurs. However, since ray tracing only tracks the primary direction of energy flow and typically does not account for diffraction, it provides an incomplete understanding of the interaction of HF waves with small ionospheric irregularities. This work investigates the orthogonality assumptions by modeling at high-resolution HF electromagnetic wave interactions with small-scale irregularities in the ionosphere. Specifically, the finite-difference time-domain (FDTD) method is employed to determine where orthogonality occurs in the ionosphere and the number of times the condition is satisfied during the simulation. The results provide insights into the orthogonality condition as a function of source frequency and elevation angle for both unperturbed and perturbed ionospheres. From these results, small-scale irregularities are observed to sometimes contribute significantly to the production of backscatter. A discussion is provided to highlight where three existing orthogonality condition assumptions are incorrect or misleading.

## 1. Introduction

For the last couple of decades, Super Dual Auroral Radar Network (SuperDARN) radars (Chisham et al., 2007; Greenwald et al., 1995) have been monitoring high-latitude plasma in the ionosphere. The network consists of 35 (as of April 2020) high-frequency (HF: 8–20 MHz) radars that are located around the globe. The primary focus of SuperDARN is to map the plasma dynamics on a global scale. However, it has also proven successful in investigating the Earth's natural phenomena in the magnetosphere, thermosphere, and mesosphere. For example, SuperDARN has been helpful in studying field-aligned currents (Moen et al., 2013), magnetic reconnection (Zhang et al., 2012), magnetic storms (Oksavik et al., 2006), magnetohydrodynamic waves (Chisham et al., 2007), gravity waves (Hall et al., 1999), and high-latitude plasma structures such as polar cap patches (Carlson, 2012; Hosokawa et al., 2001; Ogawa et al., 2009).

For SuperDARN's radars to monitor high-latitude ionospheric plasma convection, the radars must receive coherent backscatter generated in the *F* region of the ionosphere. The line-of-sight backscatter contains information about Doppler frequency shifts caused by irregularity plasma structures (Ponomarenko, 2009). These Doppler frequency shifts are then used to deduce the plasma drift velocity. It is crucial to have accurate knowledge of where the ionospheric backscatter occurs when performing analyses under the following scenarios: (1) in studies of small and mesoscale velocity structures; (2) studies of plasma evolution and instabilities; and (3) when comparing SuperDARN measurement results with those obtained from space-based instruments and ground-based instruments (Chisham et al., 2008). However, being able to obtain accurate ionospheric backscatter depends on having accurate knowledge of the propagation paths of the HF signals in the complex ionosphere (Greenwald et al., 2017).

The propagation of HF radio waves is heavily impacted by the composition of the ionosphere because the plasma frequency, gyrofrequency, and frequency of the radio waves are all very comparable (Smith et al., 2020). The background ionosphere causes radio waves at frequencies higher than HF, that is, very high frequency (VHF: 30–300 MHz) and ultrahigh frequency (UHF: 300 MHz to 3 GHz) waves, to transmit through the ionosphere, and lower-frequency waves, that is, low-frequency (LF: 30–300 kHz) and medium-frequency (MF: 300 kHz to 3 MHz) waves, to reflect (Liu et al., 2012). HF waves, however, experience considerable refraction due to the background ionosphere. Also, small variations in the ionosphere can generate HF backscatter. These small ionospheric variations are caused by plasma irregularities that temporally exist in the ionosphere. They are a result of convection, which causes plasma instabilities to form anisotropic magnetic field-aligned structures that can be characterized as elongated slivers with steep plasma gradients. These elongated slivers can range in horizontal length from centimeters to tens of kilometers (Bust & Crowley, 2007).

The theory of ionospheric backscatter was introduced by Booker (1956), who demonstrated that maximum scattering is dependent on the irregularity: size, electron density, and shape/orientation with respect to the direction and frequency of incident wave propagation.

With regard to the irregularity sizes, according to Bragg's scattering conditions, the maximum scattering occurs when an object is twice the length of the incident wavelength of the electromagnetic wave. In this case, the scattering object produces constructive interference allowing for wide angle diffraction. Since SuperDARN operates in the HF range from 8–20 MHz (Greenwald et al., 1985), the propagation wavelengths range from ~15–37.5 m in free space. The Bragg scale range is then 30–75 m for irregularities to produce optimal scattering. (The free space wavelength was utilized in this estimation because for a maximum electron density of ~9.0E4 $cm^{-3}$ in the ionosphere, the wavelengths corresponding to 8–20 MHz waves change by less than 2% (Smith et al., 2020).

With regard to the irregularity electron density, the relative density of the irregularities can range from 2–10 times the electron density of the ambient ionosphere (Weber et al., 1984). This intensity significantly perturbs the ionosphere and may cause the HF electromagnetic waves to experience refraction.

With regard to the irregularity shapes/orientations, the shapes of the irregularities are elongated plasma structures aligned with the magnetic field of the Earth. The maximum backscattering can occur when the incident wave is directed normal to the irregularities and hence normal to the magnetic field (Greenwald et al., 1985). This is defined as the "orthogonality condition." This means that at low and middle latitudes, the HF wave does not need to refract much before the orthogonality condition is satisfied. The orientation of the irregularities at high latitudes, however, makes it difficult for maximum backscatter to be achieved since the magnetic field is oriented radially outward (more vertically) (Chisham et al., 2008).

The orthogonality condition was introduced by Bates and Albee (1970). They demonstrated and found that at high latitudes, *F* layer echoes or backscatter were produced for off-perpendicular angles from the magnetic field of less than 5°. Thus, it was concluded that the HF waves must experience significant refraction in the ionosphere before the wave propagation direction becomes perpendicular to the magnetic field. Figure 1 is a similar diagram from Bates and Albee (1970) that illustrates how the HF waves are refracted in the ionosphere at high latitudes.

Follow-on work relating to the orthogonality condition has led to three assumptions under which HF waves are expected to reach orthogonality with respect to the background magnetic field (hereafter referred to as "orthogonality condition assumptions"): (1) the angle of elevation for the incident wave must be low (Ponomarenko, 2009); (2) it takes considerable horizontal distance in the ionosphere for the wave to refract enough to reach orthogonality (Liu et al., 2012); (3) orthogonality is only reached within a very narrow (in the horizontal direction) "scattering region" in the ionosphere (Bates & Albee, 1970).

The goal of this paper is to determine whether the above orthogonality condition assumptions are valid and under what conditions they hold. To accomplish this goal, high-resolution finite-difference time-domain (FDTD) (Taflove & Hagness, 2005; Yee, 1966) models are used to study the interaction of HF waves with a perturbed versus unperturbed *F* region profiles of the ionosphere. The FDTD model accounts for all of the physics of electromagnetic wave interactions with cold magnetized ionospheric plasma. As part of this investigation, FDTD is used to

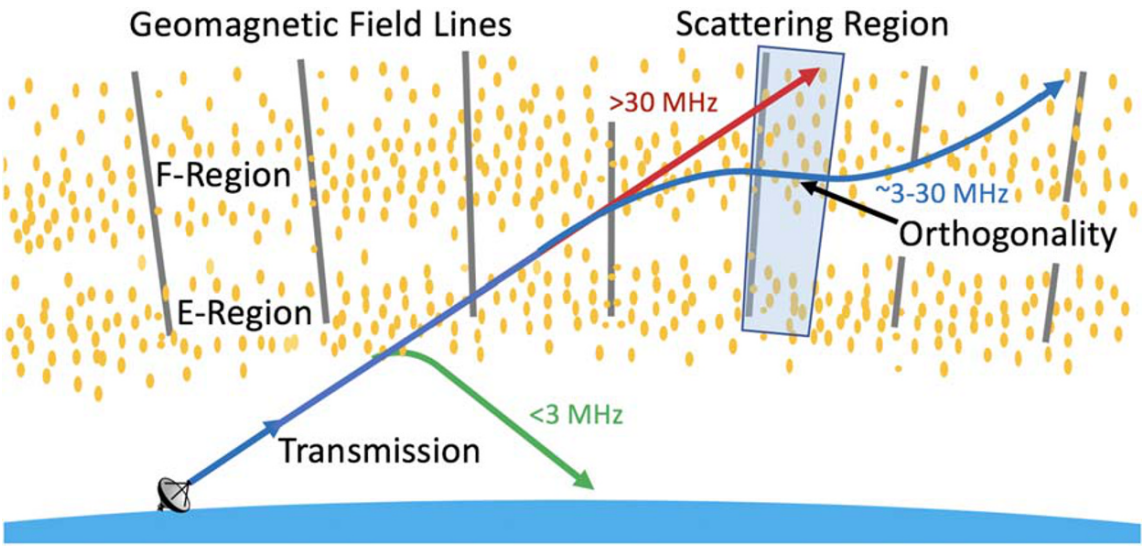


**Figure 1.** A diagram illustrating the path that HF electromagnetic waves experience at high latitudes to generate backscatter. The electromagnetic waves propagating at low-elevation angles experience considerable refraction in the ionosphere. Eventually, if the waves refract enough to reach orthogonality, at which point the wave vector is orthogonal to the magnetic field, then maximum backscattering occurs. The narrow "scattering region" is related to one of the orthogonality condition assumptions discussed in (Bates & Albee, 1970). The figure is adapted from Figure 1 of Bates and Albee (1970).

1. Calculate the transmission coefficient for an unperturbed versus a perturbed ionosphere: Details of the transmission coefficient over a range of frequencies and elevation angles for HF waves propagating in an unperturbed versus perturbed ionosphere provides intuition on how HF waves interact with the ionosphere. The transmission coefficient plots will demonstrate that the presence of ionospheric perturbations on average reduces the wave transmission.
2. Count the locations and moments in time that the HF wave is orthogonal to the background magnetic field in an unperturbed versus perturbed ionosphere: This "orthogonality count" is performed over a range of frequencies and elevation angles to determine which angles and frequencies produce the most backscatter. These FDTD-calculated results will be used to examine and analyze the orthogonality condition assumptions.

The modeling in this paper is unique because it is run at a sufficiently high resolution to examine how small-scale irregularities that are comparable to the HF's wavelength affect the backscattering of the signal. To the author's knowledge, ray tracing models of HF waves with ionospheric irregularities are run at a coarse resolution (Bernhardt et al., 2014; Cervera & Harris, 2014; Chisham et al., 2008; Greenwald et al., 1995; Liu et al., 2012). The modeling results in this paper will show that these small-scale irregularities, which are accounted for in the FDTD model, have a significant impact on where orthogonality occurs.

The remainder of this paper is organized as follows: Section 2 discusses the FDTD model setup. Section 3 discusses the ionospheric profiles for the unperturbed and perturbed ionospheres. Sections 4 and 5 describe the FDTD modeling results for the transmission coefficient and orthogonality studies. Section 6 provides a discussion of the results and how they relate to the three orthogonality condition assumptions. Section 7 summarizes and concludes the paper.

## 2. The FDTD Model

Figure 2 shows a diagram of the FDTD grid. The FDTD model extends $125 \times 10 \times 125$ km in the $X$, $Y$, and $Z$ directions, respectively. $Z$ is altitude, and the $X$ and $Y$ directions are arbitrary (east-west vs. south-north) since the magnetic field is assumed to be vertical and the orientation of $X$ and $Y$ may be defined according to the orientation of the specific radar beam of interest. The grid resolution is 2 m in all Cartesian directions (i.e., $\Delta X = \Delta Y = \Delta Z = 2$ m). This grid resolution is chosen to ensure there are at least 10 grid cells per wavelength across all frequencies of interest throughout the modeled ionosphere. This grid resolution of 2 m does

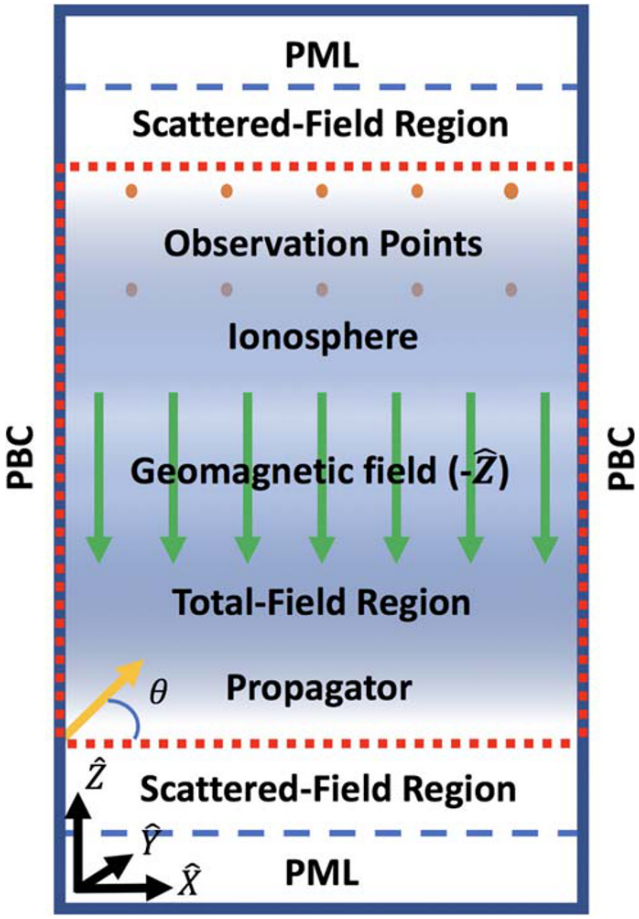


**Figure 2.** 2-D vertical slice of the fully 3-D FDTD grid having PML absorbing boundary conditions on the top and bottom and PBCs connecting the left and right sides. The red dotted lines represent the edges of the total-field region of the TFSF plane wave source formulation. The plane wave source is incident from the bottom of the grid (from the ground) and propagates at an elevation angle, $\theta$, with respect to the *X*-*Y* plane. Observation points (orange dots) are placed near the top to capture the electric fields at various locations. The geomagnetic field lines are shown as green arrows pointing in the $-Z$ direction.

limit the size of the smallest irregularities that may be modeled in the grid. In the *Z* direction, the model extends from an altitude of 250 to 375 km in the *F* region of the ionosphere. Starting the grid at 250 km makes the FDTD simulation more computationally feasible than starting it at ground level. The FDTD models are parallelized to run on 5,000 processors of a supercomputer using message passing interface.

The source is modeled as a plane wave because the *F* region of the ionosphere is in the far-field of the ground antenna by the time it propagates to an altitude of 250 km (the altitude of the bottom of the FDTD grid). To generate a plane wave, the FDTD model utilizes a total-field/scattered-field formulation with a 1-D multipoint auxiliary source propagator (Tan & Potter, 2007, 2010). The total-field region extends to the edges of the grid in the *X* and *Y* directions and 25 cells above the bottom (*Z*−) and below the top (Z+) edges of the grid. The direction of the plane wave is determined by the elevation angle, $\theta$, with respect to the *X*-*Y* plane.

The edges of the grid in the *X* and *Y* directions also have periodic boundary conditions (PBCs) that represent the continuation of the ionosphere in the horizontal directions. The PBCs are needed to keep the size of the simulation reasonable and also because both analytical (e.g., Yu & Simpson, 2011) and perfectly matched layer boundary conditions (PML) developed to-date show instabilities or have not yet been applied to spatially varying ionospheric plasma as for the *X* and *Y* sides of the grid (see, e.g., Chevalier et al., 2006). Finally, the FDTD model includes convolutional PMLs on the top and bottom (*Z* edges) free-space regions of the grid to absorb any scattered electromagnetic waves and eliminate any reflection from the *Z* boundaries (Berenger, 1994; Roden & Gedney, 2000; Taflove & Hagness, 2005).

Observation points are included in the FDTD grid to study the reflection and transmission through the *F* region of the ionosphere. 5,000 observation points are placed toward the top of the grid but before the PML boundary at 370 km in altitude. The $E_x$, $E_y$, and $E_z$ components are recorded at every time-step at the observation points.

Two types of time-dependent source waveforms are used. The first source waveform is a Gaussian modulating a sinusoidal pulse having a bandwidth of 15 MHz centered at 8 MHz. This type of source is used to investigate the power transmission through the ionosphere. The second source waveform is a sinusoid that is used to investigate the orthogonality condition. Frequencies from 1–13 MHz are used to probe the ionosphere. The wavelengths corresponding to these frequencies range from 300 to 23 m, which will be comparable to the sizes of the irregularities in the grid. The simulated electromagnetic frequencies are comparable to SuperDARN, which operates from 8 to 20 MHz.

As in Smith et al. (2020), the FDTD model couples the plasma momentum equation to Maxwell's equations (Pokhrel et al., 2018). The plasma momentum equation accounts for all ionospheric effects on the propagation of electromagnetic waves, including absorption, refraction, phase and group delay, frequency shift, polarization, and Faraday rotation. Only electrons are modeled in the plasma since the ions are primarily motionless under the short time scales of the simulation. The model simulates 35 μs in real time. Thus, the plasma momentum, shown in Equation 1, is obtained assuming a constant electron density. That is, the current densities in Equation 1 are initialized to zero, and the electron density profiles, which are discussed in section 3, are held constant in time throughout the simulation. Note that in Equation 1, $J_e$ represents the plasma current density, $\nu_e$ is the collision frequency, ε is the electrical permittivity of the medium, $\omega_{pe}$ is the plasma angular frequency, and $\omega_B$ is the cyclotron angular frequency.

$$\frac{\partial \vec{J}_e}{\partial t} + \nu_e \vec{J}_e = \varepsilon \omega_{pe}^2 \vec{E} - \vec{\omega}_B \times \vec{J}_e \tag{1}$$

The Earth's magnetic field has an amplitude of $B = 50$ μT and is oriented along the vertical ($-Z$) direction uniformly since the dip angle variation is insignificant over the horizontal extent of the model. The Earth's magnetic field shows up in the cyclotron frequency, as described in 2, where $q$ is the charge of an electron, $m$ is the mass of the electron, and $f_B$ is the cyclotron frequency. The cyclotron resonance influences the propagation of the electromagnetic waves when the cyclotron frequency is comparable to or greater than the plasma frequency and frequency of the electromagnetic wave.

$$\omega_B = 2\pi f_B = \frac{qB}{m} \tag{2}$$

Maxwell's equations and the plasma momentum equation are updated using time step increments, $\Delta t$ and $\Delta t_c$, respectively, both set to 1.0 ns. This value is chosen to satisfy the Courant limit (the upper limit of the allowable time-stepping increment for solving Maxwell's equations using FDTD to ensure numerical stability) shown in 3 for free space (Taflove & Hagness, 2005) as well as the magnetized plasma stability conditions shown in 4 and 5 (Pokhrel et al., 2018). In 3, $c$ is the speed of light in free space and $\Delta x$, $\Delta y$, and $\Delta z$ are the grid cell dimensions for the FDTD model. These conditions ensure the model avoids numerical dispersion and instabilities. In 4 and 5, the plasma frequency and cyclotron frequency must satisfy the Nyquist sampling theorem, where the sampling frequency should be at least twice the highest-frequency component (collisions at these altitudes may be neglected):

$$\Delta t < \frac{1}{c} \frac{1}{\sqrt{\frac{1}{\Delta x^2} + \frac{1}{\Delta y^2} + \frac{1}{\Delta z^2}}} \tag{3}$$

$$\Delta t < \frac{1}{2\omega_B} \tag{4}$$

$$\Delta t < \frac{1}{2\omega_{pe}} \tag{5}$$

## 3. The Ionospheric Profiles

Ionospheric profiles analogous to those described in Smith et al. (2020) are utilized. A brief description of them is included here. One difference for the FDTD models and ionospheric profiles in this paper is that they only extend up to 375 km rather than to an altitude of 450 km as in Smith et al. (2020). Two types of ionosphere profiles are modeled: an unperturbed ionosphere and a perturbed (having irregularities) ionosphere. The unperturbed profile is a simple Gaussian function with a wide distribution. The model starts at 250 km in altitude, and the profile peaks at 350 km, corresponding to the $F$ region peak in the ionosphere.

The perturbed ionosphere includes irregularities that are extracted from Defense Meteorological Satellite System (DMSP) data that captured a polar cap patch at high latitudes of the Earth on 11 December 2009. The DMSP data are obtained from three satellites (F15, F16, and F17) that provide the electron density composition along a line of sight as a function of time. The satellites have a sampling rate of either 1 s (as is the case for F16 and F17) or 4 s (for F15). The irregularities in the polar cap patch are seen in the electron density data as steep gradients with a higher density than the background ionosphere. Due to the 1 or 4 s sampling rate, the smallest structures or irregularities that the satellites can capture range from 15 to 60 km in length. However, based on observed wave backscatter, the expected lengths of the irregularities within a physical patch extend well below 15 km and even down to cm in scale (Bust & Crowley, 2007).

The irregularities observed in the DMSP data are analyzed and used to generate a histogram of the sizes of the irregularities within the polar cap patch. The distribution size of the irregularities follows a Weibull distribution, which is commonly used for particle size distributions. The fitted Weibull function is extrapolated down to 10 m to obtain the number of the smaller irregularities below 15 km to capture the wide range of irregularity sizes. A cumulative distribution function is then obtained by taking the integral of the

normalized Weibull distribution function. The cumulative distribution function describes the horizontal length distribution of irregularities that exist within the polar cap patch. This process is explained in more detail in Smith et al. (2020), which includes a figure of the histogram and the fitted Weibull distribution function.

The modeled polar cap patch is populated with irregularities from the cumulative distribution function using the resolution of the FDTD grid cells (2 m) and the size of the grid (125 × 10 × 125 km in the *X*, *Y*, and *Z* directions, respectively). A total of 15 irregularity sizes are modeled in the FDTD grid ranging from 2 m (corresponding to the size of one grid cell) to 6 km. The largest irregularity that is currently modeled is limited to 6 km based on the width of the FDTD model.

After the irregularities are determined by the cumulative distribution function for a specific grid size and resolution, the plasma density is assigned to each irregularity using a Gaussian distribution. The distribution is proportional to the size of the irregularity. In this study, to match the DMSP data, a low-density polar cap patch is modeled with irregularities having a range of densities that are a factor of one to three times the background. The irregularity structures are then subtracted from the ionospheric background as negative perturbations.

For the profiles, the ionospheric background represents the *F* region of the ionosphere and may be roughly approximated by a Gaussian distribution. The background electron concentration in the polar region has a density of ~9.0E4 $cm^{-3}$, which is equivalent to a plasma frequency of ~2.7 MHz. Figure 3 shows the 1-D background ionosphere (unperturbed ionosphere). In the profiles, the electron density peaks at around 350 km in altitude and has a standard deviation of 200 km corresponding to the ionosphere's *F* region. Figure 3b shows the 2-D perturbed ionosphere with its irregularities. The profiles were then incorporated into the FDTD model to model the HF wave interaction with the unperturbed and perturbed ionosphere profiles.

## 4. Transmission Coefficient Results

Two types of FDTD models are run in parallel: (1) a free space model and (2) one that includes the profiles generated in section 3. With regard to (2), the following three ionospheric profiles are separately simulated: an unperturbed ionosphere without a magnetic field, an unperturbed ionosphere with a 50 μT magnetic field, and a perturbed ionosphere with a 50 μT magnetic field.

The electric field at the observation points in the free-space and ionosphere profile models are recorded and transformed into the frequency domain using the discrete Fourier transform. This was done for each electric field component, that is, $E_x$, $E_y$, and $E_z$, to obtain the combined magnitude. The transmission coefficients are then calculated by taking the ratio of the electric field magnitudes in the ionospheric profile models ($E_I$) and the free-space model ($E_F$), as shown in 6.

$$\Gamma = \frac{E_I}{E_F} \tag{6}$$

In these simulations, the source is a time-dependent plane wave as a Gaussian pulse modulating a sinusoid. The elevation angle of the source ($\theta$) ranges from 15–90° in increments of 1°. Figure 4 graphs the FDTD-calculated transmission coefficient for an unperturbed ionosphere profile without a background magnetic field, and Figure 4b graphs the transmission coefficient for an unperturbed ionosphere with a background magnetic field of 50 μT. For comparison, analytical results are calculated using the dispersion relationship of the Appleton and Hartree equation. The analytical results are shown as red circles.

Figures 4a and 4b show good agreement between the FDTD-calculated transmission coefficients and the dispersion relationship from the Appleton and Hartree equation. For example, in Figure 4, when the elevation angle is 90°, or the incident plane wave propagates straight upward, the FDTD results exhibit a cutoff frequency of 2.7 MHz that matches the critical frequency of the ionosphere. In Figure 4b when the angle of elevation is 90°, the FDTD results exhibit cutoff frequencies of 2 and 3.5 MHz, which match well with the analytically calculated cutoff frequencies for the right-hand polarization (RHP) and left-hand polarization (LHP) waves, respectively.

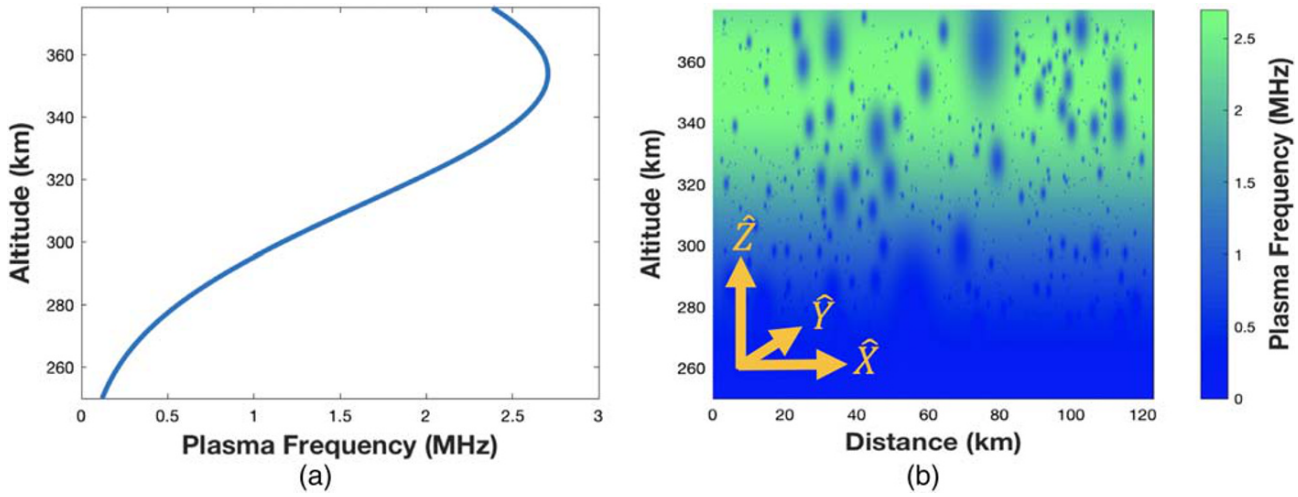


**Figure 3.** 1-D variation in altitude of the modeled 3-D unperturbed ionosphere profile representing the lower *F* region of the ionosphere (a). 2-D slice of the modeled 3-D perturbed ionosphere with a polar cap patch with its irregularities (b). The color scheme corresponds to the plasma frequency.

In both Figures 4a and 4b the transmission coefficient is seen to gradually increase at higher frequencies for low-elevation angles. Also, Figures 4a and 4b show that at high-elevation angles the transmission is more binary, whereas for lower-elevation angles the transmission coefficient increases from 0 to 1.0 smoothly over a range of frequencies. Lastly, in Figure 4b, since the plasma is magnetized, the low-frequency whistler mode is generated in the FDTD model. The whistler mode wave is most prevalent for vertical propagation at frequencies of less than ~1 MHz. For the remainder of this paper the analytical results in Figure 4 are known as the transmission/reflection boundary.

Next, the FDTD model is used to obtain the transmission coefficient for the perturbed ionosphere, where the irregularities from a polar cap patch are superimposed into the background ionosphere. A magnetic field of strength 50 μT is included, and it is aligned in the negative *Z*- direction. Following the same procedure as for Figure 4, Figure 5 shows the transmission coefficient for the perturbed ionosphere. Now, however, because the ionosphere is no longer homogeneous at each altitude, the transmission coefficient changes depending on the location of the observation point. Figure 5a shows the average transmission coefficient using data from all of 5,000 observation points, whereas Figure 5b shows the transmission coefficient obtained at a single observation point at 370 km in altitude.

In Figure 5a, the average transmission coefficient has similar properties as the results shown in Figure 4b for the unperturbed ionosphere. The streaks appearing in Figure 5b are produced by the HF waves interacting with the irregularities, which causes the HF waves to diffract and scatter in a complex manner. Also, in Figure 5b, and to a lesser extent in Figure 5a, the transmission coefficient at specific angles and frequencies is higher than unity. This is due to constructive interference that is happening between all the scattered waves at the observation point(s). In Figure 5a, the average transmission coefficients in the transmission region is nearly 0.9, compared to 1.0 for the unperturbed ionosphere, as shown in Figure 4b. The power loss indicates that 10% of the wave is scattered by the irregularities back toward the ground as HF backscatter. This 10% level of backscatter even occurs for high-elevation angles, which is parallel to both the geomagnetic field and elongation direction of the plasma irregularities.

## 5. Results for the Orthogonality Condition

HF waves experience a different amount of refraction in the ionosphere depending on their altitude, spectral composition, and propagation direction relative to the background magnetic field. These three factors also influence when a propagating HF wave might reach orthogonality with respect to the background magnetic field, at which point a maximum amount of backscatter is expected to be produced.

In this section, FDTD modeling is performed to study in detail where the orthogonality condition is reached for different frequencies and angles of incidence on the ionosphere. For these simulations, the plane wave

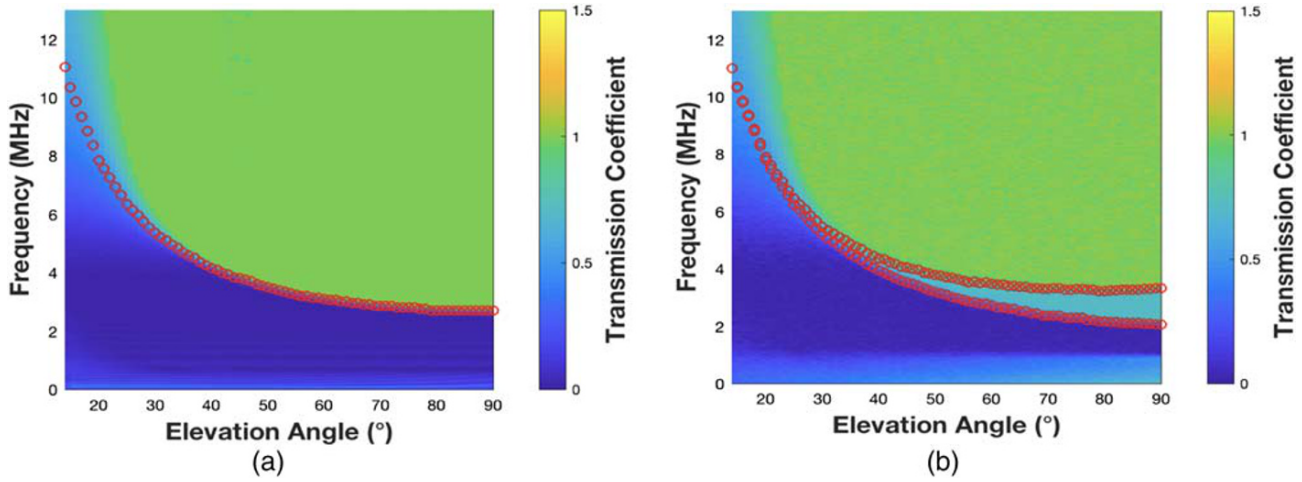


**Figure 4.** Plots of the FDTD-calculated transmission coefficient as a function of frequency and elevation angle for an unperturbed ionosphere without a background magnetic field (a) and with a magnetic field of 50 μT (b). For comparison, analytical results are shown as red circles. In Figure 4b, the red circles follow two lines, representing the left-hand polarization (LHP) and right-hand polarization (RHP) waves. The largest amount of backscatter is generated for the source frequencies and elevation angles having a transmission ratio of zero (dark blue region).

source is a sinusoidal time waveform. The simulation is rerun for different frequencies and different elevation angles. At every time step and grid cell, the Poynting vector of the electromagnetic wave is calculated using Equations 6, 7a, and 7b:

$$S_x = \left[E_y\big|^n_{i+\frac{1}{2},j,k+\frac{1}{2}}\right]\left[\left(H_z\big|^n_{i,j,k+\frac{1}{2}} + H_z\big|^n_{i+1,j,k+\frac{1}{2}}\right)/2\right] - \left[E_z\big|^n_{i+\frac{1}{2},j+\frac{1}{2},k}\right]\left[\left(H_y\big|^n_{i,j+\frac{1}{2},k} + H_y\big|^n_{i+1,j+\frac{1}{2},k}\right)/2\right] \quad (6a)$$

$$S_y = -\left[E_x\big|^n_{i,j+\frac{1}{2},k+\frac{1}{2}}\right]\left[\left(H_z\big|^n_{i,j,k+\frac{1}{2}} + H_z\big|^n_{i,j+1,k+\frac{1}{2}}\right)/2\right] - \left[E_z\big|^n_{i+\frac{1}{2},j+\frac{1}{2},k}\right]\left[\left(H_x\big|^n_{i+\frac{1}{2},j,k} + H_x\big|^n_{i+\frac{1}{2},j+1,k}\right)/2\right] \quad (6b)$$

$$S_z = \left[E_x\big|^n_{i,j+\frac{1}{2},k+\frac{1}{2}}\right]\left[\left(H_y\big|^n_{i,j+\frac{1}{2},k} + H_y\big|^n_{i,j+\frac{1}{2},k+1}\right)/2\right] - \left[E_y\big|^n_{i+\frac{1}{2},j,k+\frac{1}{2}}\right]\left[\left(H_x\big|^n_{i+\frac{1}{2},j,k} + H_x\big|^n_{i+\frac{1}{2},j,k+1}\right)/2\right] \quad (6c)$$

$$\theta = \tan^{-1}\left(\frac{S_z}{S_x}\right) \quad (7a)$$

$$\varphi = \tan^{-1}\left(\frac{S_z}{S_y}\right) \quad (7b)$$

where $S_x$, $S_y$, and $S_z$ are the Poynting vectors for each Cartesian direction, $E_x$, $E_y$, $E_z$ and $H_x$, $H_y$, $H_z$ are the electric and magnetic field components, $\theta$ is the elevation angle the Poynting vector makes with the $X$ axis, and $\varphi$ is the elevation angle the Poynting vector makes with respect to the $Y$ axis. To obtain the magnetic field in all three Cartesian directions at the same position in space, two of the magnetic field components are averaged in space, since all of the field components are offset in space by half a of grid cell (Moerloose & Zutter, 1995). The angles $\theta$ and $\varphi$ of the Poynting vector at each grid cell and at each time-step are calculated using Equations 7a and 7b. Each moment in space and time that the angle of the wave is within ±0.5° of orthogonality (at 0°, pointing parallel to the $X$-$Y$ plane), a counter in the model increases by one. Each simulation having a different source frequency and elevation angle has a separate counter for the number of times the orthogonality condition is met throughout the space and time of the simulation.

Figure 6 shows the number of times that the orthogonality condition is met for all of the simulations (different source frequencies and elevation angles) having the unperturbed magnetized ionosphere profile shown in Figure 3. As expected, low-elevation angles are seen to refract in the ionosphere and reach orthogonality more than higher-elevation angles. Further, for each elevation angle, the orthogonality condition is met most often near the transmission/reflection boundary (shown in Figure 4).

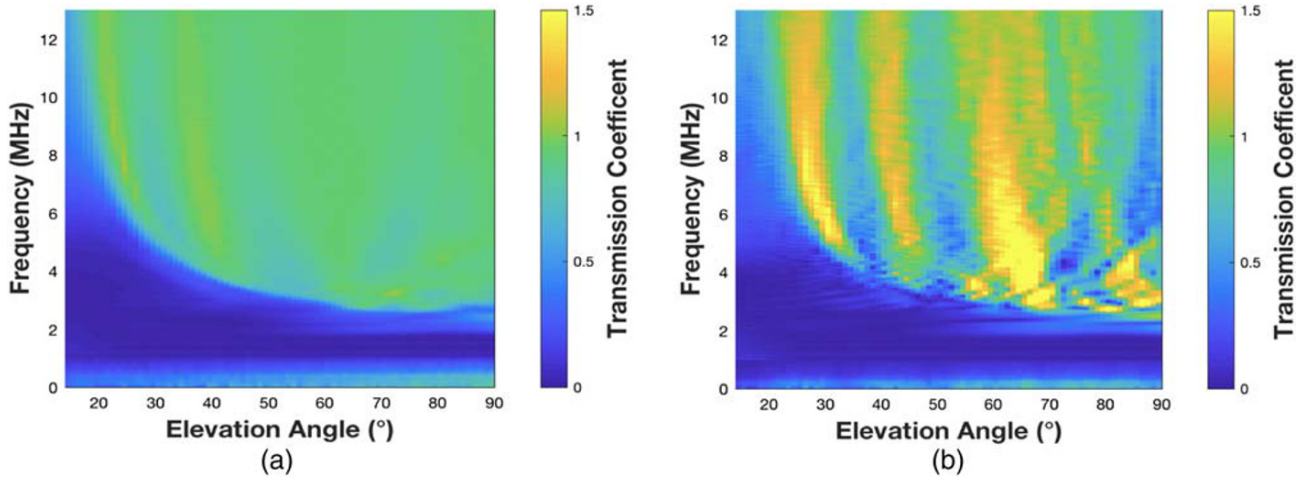


**Figure 5.** Transmission coefficient for a perturbed ionosphere with a background magnetic field of 50 μT. Figure 5a is the average transmission coefficient calculated from 5,000 observation points. Figure 5b shows the transmission coefficient as calculated at a single observation point. The average transmission coefficient is 0.9 in the transmission region, indicating that 10% of the wave is reflected or scattered back.

Figure 6b shows the number of times that the orthogonality condition is met for all of the simulations (different source frequencies and elevation angles) having the perturbed magnetized ionosphere profile shown in Figure 3b. As for Figure 6, Figure 6b shows that low-source elevation angles refract in the ionosphere and reach orthogonality more than higher-source elevation angles, even for a perturbed ionosphere. However, comparing Figures 6a and 6b, Figure 6b shows a significantly higher number of orthogonality conditions occur for high-source elevation angles. This is due to the small-scale irregularities that can cause the HF waves to refract significantly over a relatively short propagation distance. The red asterisks in Figure 6b indicate the specific angles and frequencies at which data are extracted to produce Figures 7a–7d. Figure 6b is interesting as it shows that the HF waves for all source elevation angles and frequencies beyond the transmission/reflection boundary can reach orthogonality.

Figures 7a–7d maps where orthogonality occurs for various source elevation angles at 2.5 MHz. Figures 7a–7d first show 2-D vertical (*XZ*) slices of the perturbed ionosphere profile. Figure 7a corresponds to the simulation with a 20° source elevation angle, Figure 7b has a 40° elevation angle, Figure 7c has a 60° elevation angle, and Figure 7d has an 80° elevation angle. The red-filled circles correspond to the specific locations where the Poynting vector is orthogonal to the background magnetic field. The size of the red circles correspond to the number of times orthogonality occurs at that grid cell during the time span of the simulation. In Figure 7a, the total orthogonality count is 35,384; Figure 7b has an orthogonality count of 13,182; Figure 7c has an orthogonality count of 12,188; and Figure 7d has an orthogonality count of 31,510. Figure 7a shows that the orthogonality condition is met more equally throughout the region between ∼290 and 310 km in altitude because all the red circles are roughly the same size. However, in Figure 7d, there are fewer red circles, but the circles are larger and are more concentrated around the irregularities. This indicates that for higher-elevation angles, whether the wave reaches orthogonality is more dependent on the small-scale irregularities rather than on the background ionosphere profile.

## 6. Discussion

For the last couple of decades, SuperDARN has been successful at examining physical processes in the magnetosphere, ionosphere, thermosphere, and mesosphere (Chisham et al., 2007). One area of focus is the plasma entry and convection across the polar region of the Earth. To study this phenomenon, SuperDARN's radars use HF waves directed toward the plasma irregularities in the area and then capture the backscatter that returns. The backscatter contains useful information, such as Doppler frequency shifts that may be used to map and define the irregularities in the ionosphere.

Many numerical methods have been used to study the backscattering process and better map the location of irregularities from observed data (Bernhardt et al., 2014; Cervera & Harris, 2014; Chisham et al., 2008;

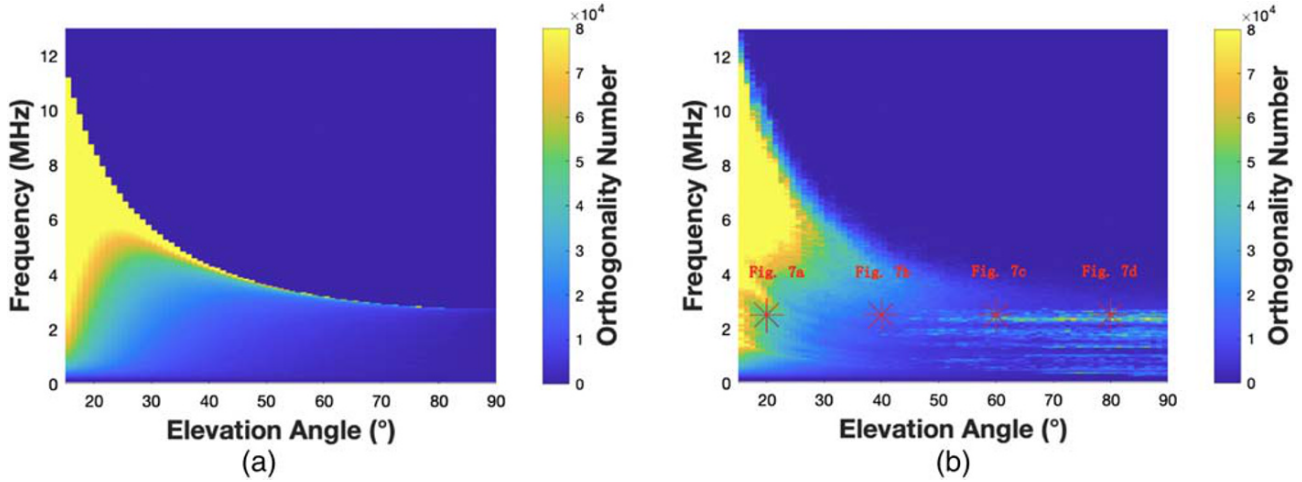


**Figure 6.** The number of times that the orthogonality condition is met for all of the simulations (different source frequencies and elevation angles) having the unperturbed (a) and perturbed (b) magnetized ionosphere profile shown in Figures 3 and 3b, respectively. The color scheme is the number of times the orthogonality condition is met throughout the spatial domain of the grid and time span of each simulation. As expected, low-source elevation angles reach orthogonality more easily than higher-source elevation angles. The red asterisks indicate the specific angles and frequencies at which data are extracted to produce Figures 7a–7d.

Greenwald et al., 1995; Liu et al., 2012). The majority of these models are based on ray tracing, an approach that treats the HF waves as rays and only tracks the primary direction of energy flow. For these models to be sufficiently accurate, two conditions must be satisfied. First, the spatial resolution must be less than the Fresnel diffraction scale (Bernhardt et al., 2014; Rino, 2011). Second, any material objects in the spatial domain of interest must be larger than the wavelength of the incident wave (Smith et al., 2020). If this is not the case, then wave theory, which accounts for diffraction, must be included in the calculation in order to obtain sufficient accuracy.

It is well known that ionospheric irregularities vary in size ranging from kilometers down to centimeters (Bust & Crowley, 2007). Consequently, numerical modeling of HF propagation in the ionosphere would ideally be performed at a sufficiently high resolution while also accounting for diffraction, scattering, and refraction phenomena near irregularities. Ray tracing models are at a disadvantage for not using a full-wave solver when the HF wavelengths are comparable to the irregularity sizes. However, an advantage of ray tracing is the speed at which solutions may be obtained.

The FDTD method is a robust numerical technique that accounts for diffraction by solving Maxwell's equations. It can thus accurately model electromagnetic wave interaction with irregularities on a subwavelength scale (Smith et al., 2020). Also, when coupling Maxwell's equations with the plasma momentum equation, the model accounts for all of the important physics of electromagnetic wave propagation in a magnetized ionospheric plasma, including phase and group delay, frequency shift, polarization, Faraday rotation, absorption, refraction, scatter, and diffraction (Pokhrel et al., 2018).

A maximum amount of diffraction is expected to occur when electromagnetic waves incident on the scattering objects satisfy the Bragg's condition. The ionosphere irregularities that exist in a polar cap patch are elongated along the direction of the background magnetic field. Thus, the orientation of the irregularities allows Bragg's condition to be satisfied more easily when the wave is orthogonal to the background magnetic field. Therefore, in modeling efforts, calculating where orthogonality occurs enables scientists to deduce where electromagnetic waves are scattering from irregularities in the ionosphere.

Since most modeling efforts that describe the interaction of HF waves and irregularities are based on geometric optics (ray tracing) and not a full-wave Maxwell's equations solver, the models can only accurately calculate scattering from objects much larger than the source's wavelength, and in turn disregards diffraction effects and objects that are in the Bragg's scale range. Thus, in doing so, the three orthogonality condition assumptions have been examined and investigated. The three orthogonality condition assumptions are as follows: (1) only HF waves propagating with low-elevation angles can reach orthogonality

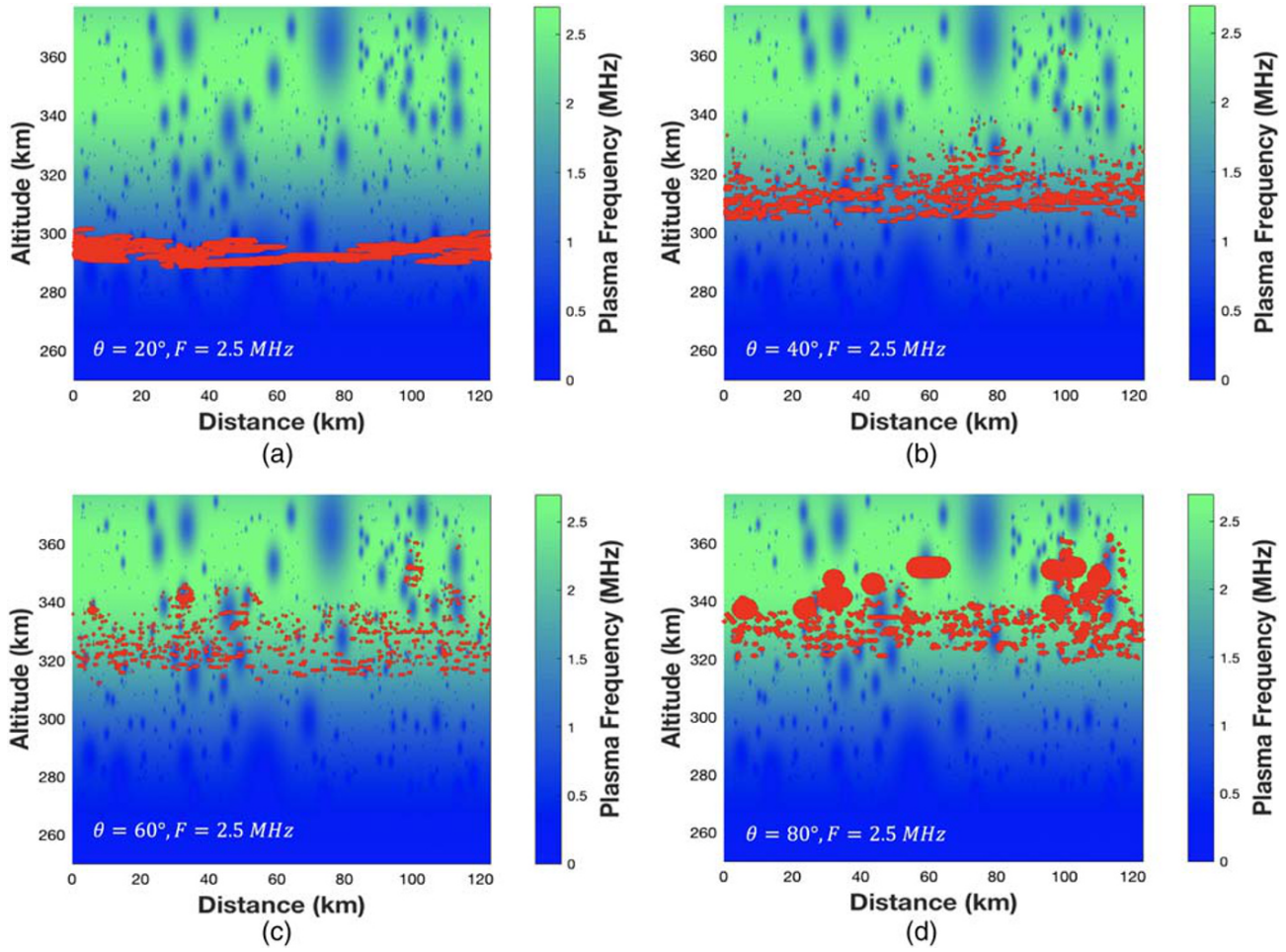


**Figure 7.** 2-D slices of the modeled 3-D perturbed ionosphere profiles. The color scheme corresponds to the plasma frequency. The red-filled circles show where orthogonality occurs. The size of the red-filled circles correspond to the number times the orthogonality condition is reached for that specific location. Figure 7a shows where orthogonality occurs for an elevation angle of 20°. Figure 7b shows where orthogonality occurs for a 40° elevation angle. Figure 7c shows where orthogonality occurs for a 60° elevation angle. Figure 7d shows where orthogonality occurs for an 80° elevation angle. The source frequency for Figures 7a–7d is 2.5 MHz.

(Ponomarenko, 2009); (2) HF waves must propagate a significant horizontal distance in the ionosphere in order to reach orthogonality (Liu et al., 2012); (3) there exists a particular horizontal region for orthogonality to occur in the ionosphere (Bates & Albee, 1970). The next three paragraphs will describe conditions under which these assumptions are shown to be incomplete and even misleading. Here, on the other hand, using FDTD modeling, all of the physics is accounted for of HF propagation interacting with irregularity structures in the ionosphere ranging in size from 10 m to 6 km. As a result, a more complete view of orthogonality is obtained.

The FDTD modeling results in Figures 6 and 7d show that the first assumption, that only low-elevation angles can reach orthogonality, is incomplete. In Figure 7, most of the orthogonality does occur for low-elevation angles; however, orthogonality also occurs for waves at specific high-elevation angles that are below the critical plasma frequency, as demonstrated in Figure 7d. The fact that orthogonality occurs at all at high elevation angles is surprising. The red circles mark where orthogonality occurs in the simulated ionosphere. The small-scale irregularities cause the HF waves to quickly refract and satisfy the orthogonality condition. It is interesting to note that in Figures 7a and 7d, the number of times the orthogonality condition is satisfied is about the same in both simulations (35,384 vs. 31,510). However, there are fewer locations that orthogonality can occur for the high-elevation angle case (Figure 7d), so those specific locations have a higher number of orthogonality counts, hence the bigger circles.

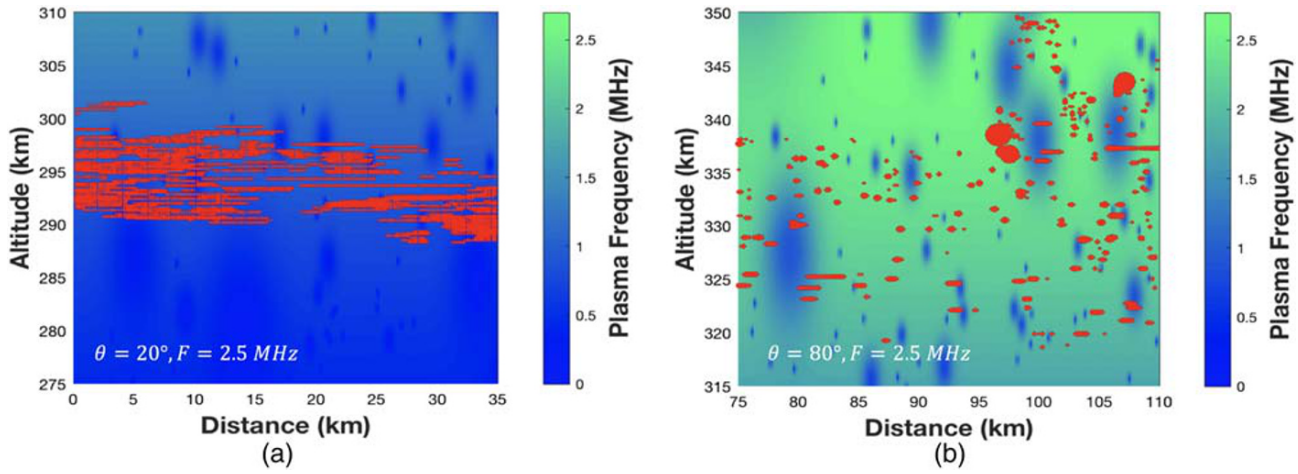


**Figure 8.** Zoomed-in views of Figures 7a and 7d, respectively. The background is a 2-D slice (*XZ* plane) through the 3-D perturbed ionosphere. The color scheme corresponds to the plasma frequency. The red-filled circles show where the orthogonality condition is satisfied at specific source elevation angles. The size of the circles indicates the number of times orthogonality is reached at that particular location. Figure 8a shows where orthogonality occurs for 20°. Figure 8b shows where orthogonality occurs for 80°. The source frequency for Figures 8a and 8b is 2.5 MHz.

The second orthogonality condition assumption says that the HF waves must propagate a significant horizontal distance in order to reach orthogonality. This signifies that refraction takes a considerable distance to finally reach orthogonality. This is depicted in Figure 1, where a low-elevation angle is refracted in the ionosphere until it achieves orthogonality. This assumption is invalid, as shown in Figure 8. Figures 8a and 8b are zoomed-in views of Figures 7a and 7d, respectively.

Figure 8 has a low-source elevation angle, where the wave is able to refract over a large distance in the ionosphere. As a result, in Figure 8a, the red circles form horizontal streaks across the ionosphere. See Figure 9 for a depiction of this type of propagation path.

On the other hand, Figure 8b has a high source elevation angle. There are no significant streaks in Figure 8b compared to Figure 8a. This indicates that the wave quickly achieved orthogonality near an irregularity and then the wave vector changed direction quickly afterward. The orthogonality counts occur close to an irregularity where there is a rapid change in the refraction index, since the source frequency (2.5 MHz) is very close to the critical frequency of the ionosphere (2.7 MHz). See Figure 9 for a depiction of the propagation path. Thus, a wave can experience significant refraction in a short distance to reach orthogonality.

According to the third orthogonality condition assumption, as shown in Figure 1, it is assumed that orthogonality occurs only over a very narrow horizontal distance (corresponding to the *X* direction in the FDTD grid) even if the irregularities are widely distributed (Bates & Albee, 1970). This is a misleading assumption as shown in Figures 7a–7d, it is observed that orthogonality occurs across a large horizontal distance (along the *X* axis) of the ionosphere and not over a very narrow horizontal distance. A large number of irregularities particularly small-scale structures affect the propagation path.

The fact that the three orthogonality condition assumptions are misleading and even invalid has been discovered through the use of an extremely high-resolution (2 m) FDTD model. This high resolution allowed for small-scale irregularities to be included in the model. The small-scale irregularities were found to influence the HF propagation, as observed in Figure 8b. These irregularities were added using a Weibull distribution that was derived in section 3 by extrapolating DMSP observed data. Ultimately, more observed data and sophisticated instruments are needed to better describe the composition of the ionosphere and the irregularity structures.

The transmission coefficients were calculated in section 4 for each ionosphere profile as a function of frequency and source elevation angle to measure the electromagnetic wave interaction with the ionosphere. Figures 4a and 4b demonstrated the model's ability to accurately calculate the transmission and reflection in an unperturbed ionosphere both with and without a background magnetic field. Analytical Appleton

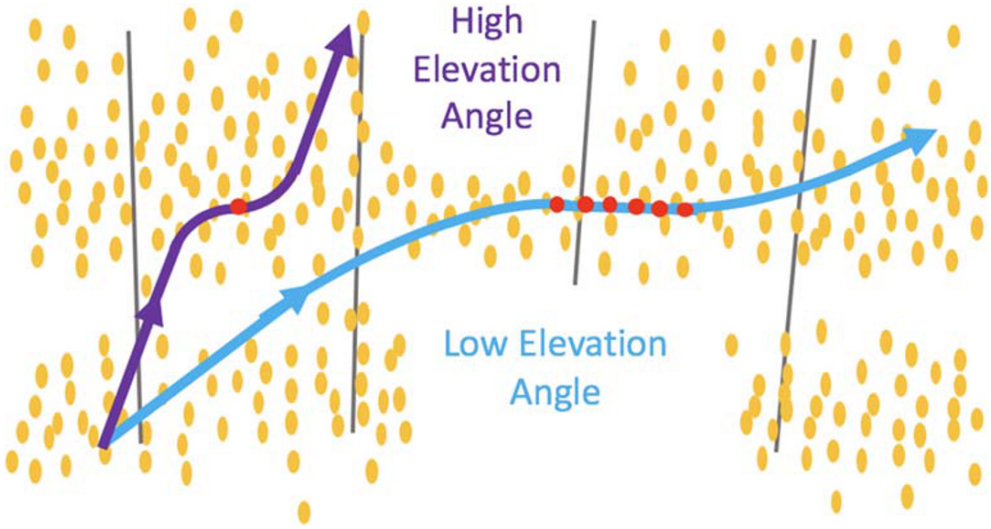


**Figure 9.** A diagram of different propagation paths. The light blue line shows the trajectory for a low-source elevation angle, that is, representing the scenario in Figure 8 where the ionosphere slowly refracts the wave to reach orthogonality (red circles), causing streaks. The purple line shows the trajectory for a high-source elevation angle, that is, representing the scenario in Figure 8b where the frequency is comparable to the critical frequency of the plasma and thus the irregularities cause quick changes in the propagation direction.

and Hartree equation results were superimposed for comparison. The transmission coefficients were then calculated for a magnetized, perturbed ionosphere at a single observation point and then averaged over 5,000 observation points. Figure 5a showed that above the transmission/reflection boundary, only 90% of the wave transmitted through the ionosphere. This indicates that 10% of the HF wave was scattered and returned to the ground. In other words, adding in the ionospheric perturbations reduced the average transmission by 10%.

The FDTD model utilized a total-field scattered-field plane wave source condition with a 1-D multipoint auxiliary source propagator (Tan & Potter, 2007). The propagator allowed for plane waves to be included in the model at various elevation angles. The model used the plasma momentum equation to account for the cold magnetized plasma using the electron densities from DMSP data. The plasma momentum equation was derived for a constant electron density since the simulation time was extremely short compared to the plasma flow. The simulations covered 35 $\mu$s in real time. The collision frequency was neglected and is approximated to zero since collisions would have little effect on the HF wave propagation in the *F* region of the ionosphere (Zawdie et al., 2017).

The FDTD models utilized source frequencies ranging from 1–13 MHz. SuperDARN uses higher frequencies of 8–20 MHz. It would be ideal to directly model the higher frequencies of SuperDARN. However, in order to directly model frequencies of 8–20 MHz, the FDTD grid spatial resolution would need to be increased by a factor of 1.5 in all three Cartesian directions (in order to maintain at least 10 grid cells per wavelength). This would necessitate a factor of 3.4 times more total processors than the current simulations in this paper (which use 5,000 processors each) in order to maintain the same number of grid cells (i.e., "work") per processor. Additionally, the time-stepping increment would need to be decreased by 35% according to (3). For this reason, in order to make the simulations more computationally feasible while studying the same electromagnetic phenomena, the FDTD models are scaled to the slightly lower frequency range of 1–13 MHz.

## 7. Conclusion and Future Work

3-D FDTD models were used to simulate HF propagation in the ionosphere over a range of frequencies and elevation angles for unmagnetized/magnetized and unperturbed/perturbed ionosphere profiles. For this study, numerous FDTD simulations were conducted with different source elevation angles and frequencies in order to determine where and when the orthogonality condition was reached and when the most backscatter would be produced. As expected, the low-elevation angle waves were able to refract and achieve

orthogonality. However, an appreciable amount of orthogonality was reached for high-elevation-angle waves. Images of the ionosphere profile were superimposed on the orthogonality condition results to demonstrate that the ionospheric perturbations were causing HF waves propagating at a high-elevation angle to reach orthogonality.

In summary, the results from the FDTD simulations improve our understanding of electromagnetic wave interaction with the ionosphere. From this work the following conclusions were made:

1. For a perturbed ionosphere, an average of 10% of the electromagnetic power is lost in the transmission due to the irregularities.
2. For an unperturbed ionosphere, the most orthogonality occurs for low-elevation angles. And for each of these low-elevation angles, the most orthogonality occurs near the transmission/reflection boundary.
3. The previous "orthogonality condition assumption" (that the angle of elevation for the incident wave must be low, Ponomarenko, 2009) is incomplete, since the FDTD model showed that high-elevation angles can reach orthogonality also.
4. Irregularities are necessary for high-elevation angles to reach orthogonality.
5. The previous "orthogonality condition assumption" (that it takes considerable horizontal distance in the ionosphere for the wave to refract enough to reach orthogonality, Liu et al., 2012) is misleading. The FDTD modeling showed that low-elevation angles cause streaks of orthogonality to occur over long horizontal distances. On the other hand, high-elevation angles caused single positions of orthogonality adjacent to the irregularities.
6. The singular positions at which orthogonality occurs adjacent to irregularities indicates that steep gradients of the electron density in the irregularities can quickly change the wave's Poynting vector.
7. The previous "orthogonality condition assumption" (that orthogonality is only reached within a very narrow [in the horizontal direction] "scattering region" in the ionosphere, Bates & Albee, 1970) is invalid, as orthogonality occurred throughout the FDTD model for every frequency and elevation angle.

Future work is needed to further improve our understanding of the interaction of electromagnetic waves with irregularities in the ionosphere. Future investigations will include a sensitivity study to examine HF backscatter from different irregularity sizes. The results may be compared with Booker's (1956) work, which describes parameters such as irregularity size, shape, magnitude, and spatial densities to produce maximum backscatter. Additionally, it will be interesting to study how the irregularity shapes, electron densities, orientations, and sizes relative to the transmitted wavelength affect the scattering of the electromagnetic waves. The FDTD model results will be compared with observed SuperDARN data.

Future work will also include studies of Doppler effects, especially in the presence of small-scale dynamic structures (which will produce Doppler spreading). That is, a moving object will no longer impart a single Doppler tone, but rather have its Doppler power spread in spectrum due to the subwavelength structures moving at different speeds. The grid-based and time-domain FDTD method can account for subwavelength structures moving at different speeds, both faster and slower than the bulk object. Furthermore, FDTD models may be used to explore how the positive and negative interference at subwavelength levels may affect Doppler information.

## Data Availability Statement

All data are available from Smith, Dallin (2020): Data for Paper2 are available from figshare. Dataset (https://doi.org/10.6084/m9.figshare.12249965).

**Acknowledgments**

This project was supported by an internship with the Air Force Research Laboratory (AFRL) Space Scholar Program and by the Universities Space Research Association (USRA). The data sets from the Defense Meteorological Satellite Program (DMSP) are greatly acknowledged. The support and resources from the Center for High Performance Computing at the University of Utah are gratefully acknowledged.

## References

Bates, H. F., & Albee, P. R. (1970). Aspect sensitivity of *F*-layer HF backscatter echoes. *Journal of Geophysical Research*, *75*(1), 165–170. https://doi.org/10.1029/JA075i001p00165

Berenger, J. P. (1994). A perfectly matched layer for the absorption of electromagnetic waves. *Journal of Computational Physics*, *114*(2), 185–200. https://doi.org/10.1006/jcph.1994.1159

Bernhardt, P. A., Hei, M. A., Siefring, C. L., & Wilkens, M. R. (2014). Predictions of HF system performance for propagation through disturbed ionospheres measured using low-earth-orbit satellite radio beacon tomography. *Radio Science*, *49*, 506–517. https://doi.org/10.1002/2014RS005409

Booker, H. G. (1956). A theory of scattering by nonisotropic irregularities with application for radar reflections from aurora. *Journal of Atmospheric and Terrestrial Physics*, *8*, 2004–2221.

Bust, G. S., & Crowley, G. (2007). Tracking of polar cap ionospheric patches using data assimilation. *Journal of Geophysical Research*, *112*, A05307. https://doi.org/10.1029/2005JA011597

Carlson, H. C. (2012). Sharpening our thinking about polar cap ionospheric patch morphology, research, and mitigation techniques. *Radio Science*, *47*, RS0L21. https://doi.org/10.1029/2011RS004946

Cervera, M. A., & Harris, T. J. (2014). Modeling ionospheric disturbance features in quasi-vertically incident ionograms using 3-D magnetoionic ray tracing and atmospheric gravity waves. *Journal of Geophysical Research: Space Physics*, *119*, 431–440. https://doi.org/10.1002/2013JA019247

Chevalier, M. W., Chevalier, T. W., & Inan, U. S. (2006). A PML utilizing k-vector information as applied to the whistler mode in a magnetized plasma. *IEEE Transactions on Antennas and Propagation*, *54*(8), 2424–2429. https://doi.org/10.1109/TAP.2006.879220

Chisham, G., Lester, M., Milan, S. E., Freeman, M. P., Bristow, W. A., Grocott, A., et al. (2007). A decade of the Super Dual Auroral Radar Network (SuperDARN): Scientific achievements, new techniques and future directions. *Surveys in Geophysics*, *28*, 33–109. https://doi.org/10.1007/s10712–007–9017–8

Chisham, G., Yeoman, T. K., & Sofko, G. J. (2008). Mapping ionospheric backscatter measured by the SuperDARN HF radars-Part 1: A new empirical virtual height model. In *Annales Geophysicae* (Vol. 26, no. 4, pp. 823–841). Germany: European Geosciences Union.

Greenwald, R. A., Baker, K. B., Dudeney, J. R., Pinnock, M., Jones, T. B., Thomas, E. C., et al. (1995). DARN/SuperDARN: A global view of the dynamics of high-latitude convection. *Space Science Reviews*, *71*, 761–795.

Greenwald, R. A., Baker, K. B., Hutchins, R. A., & Hanuise, C. (1985). An HF phased-array radar for studying small-scale structure in the high-latitude ionosphere. *Radio Science*, *20*(1), 63–79. https://doi.org/10.1029/RS020i001p00063

Greenwald, R. A., Frissell, N., & de Larquier, S. (2017). The importance of elevation angle measurements in HF radar investigations of the ionosphere. *Radio Science*, *52*, 305–320. https://doi.org/10.1002/2016RS006186

Hall, G. E., MacDougall, J. W., Cecile, J. F., Moorcroft, D. R., & St.-Maurice, J. P. (1999). Finding gravity wave source positions using the Super Dual Auroral Radar Network. *Journal of Geophysical Research*, *104*(A1), 67–78. https://doi.org/10.1029/98JA02830

Hosokawa, K., Iyemori, T., Yukimatu, A. S., & Sato, N. (2001). Source of field-aligned irregularities in the subauroral *F* region as observed by the SuperDARN radars. *Journal of Geophysical Research*, *106*(A11), 24,713–24,731. https://doi.org/10.1029/2001JA900080

Liu, E. X., Hu, H. Q., Liu, R. Y., Wu, Z. S., & Lester, M. (2012). An adjusted location model for SuperDARN backscatter echoes. *Annales Geophysicae*, *30*(12), 1769–1779. https://doi.org/10.5194/angeo-30-1769-2012

Moen, J., Oksavik, K., Alfonsi, L., Daabakk, Y., Romano, V., & Spogli, L. (2013). Space weather challenges of the polar cap ionosphere. *Journal of Space Weather and Space Climate*, *3*, A02.

Moerloose, J. D., & Zutter, D. D. (1995). Poynting's theorem for the finite-difference-time-domain method. *Microwave and Optical Technology Letters*, *8*(5), 257–260. https://doi.org/10.1002/mop.4650080512

Ogawa, T., Nishitani, N., Otsuka, Y., Shiokawa, K., Tsugawa, T., & Hosokawa, K. (2009). Medium-scale traveling ionospheric disturbances observed with the SuperDARN Hokkaido radar, all-sky imager, and GPS network and their relation to concurrent sporadic E irregularities. *Journal of Geophysical Research*, *114*, A03316. https://doi.org/10.1029/2008JA013893

Oksavik, K., Greenwald, R. A., Ruohoniemi, J. M., Hairston, M. R., Paxton, L. J., Baker, J. B. H., et al. (2006). First observations of the temporal/spatial variation of the sub-auroral polarization stream from the SuperDARN wallops HF radar. *Geophysical Research Letters*, *33*, L12104. https://doi.org/10.1029/2006GL026256

Pokhrel, S., Shankar, V., & Simpson, J. J. (2018). 3-D FDTD Modeling of electromagnetic wave propagation in magnetized plasma requiring singular updates to the current density equation. *IEEE Transactions on Antennas and Propagation*, *66*(9), 4772–4781. https://doi.org/10.1109/TAP.2018.2847601

Ponomarenko, P. V. (2009). Refractive index effects on the scatter volume location and Doppler velocity estimates of ionospheric HF backscatter echoes. *Annales Geophysicae*, *27*(11), 4207–4219.

Rino, C. (2011). *The theory of scintillation with applications in remote sensing*. New York: John Wiley & Sons. https://doi.org/10.1002/9781118010211

Roden, J. A., & Gedney, S. D. (2000). Convolution PML (CPML): An efficient FDTD implementation of the CFS–PML for arbitrary media. *Microwave and Optical Technology Letters*, *27*(5), 334–339. https://doi.org/10.1002/1098-2760(20001205)27:5<334::AID-MOP14>3.0.CO;2-A

Smith, D. R., Huang, C. Y., Dao, E., Pokhrel, S., & Simpson, J. J. (2020). FDTD modeling of HF waves through ionospheric plasma irregularities. *Journal of Geophysical Research: Space Physics*, *125*, e2019JA027499. https://doi.org/10.1029/2019JA027499

Taflove, A., & Hagness, S. C. (2005). *Computational electrodynamics: The finite-difference time-domain method*. Norwood, MA: Artech House.

Tan, T., & Potter, M. (2007). 1-D multipoint auxiliary source propagator for the total-field/scattered-field FDTD formulation. *IEEE Antennas and Wireless Propagation Letters*, *6*, 144–148. https://doi.org/10.1109/LAWP.2007.891959

Tan, T., & Potter, M. (2010). FDTD discrete plane wave (FDTD-DPW) formulation for a perfectly matched source in TFSF simulations. *IEEE Transactions on Antennas and Propagation*, *58*(8), 2641–2648. https://doi.org/10.1109/TAP.2010.2050446

Weber, E. J., Buchau, J., Moore, J. G., Sharber, R., Livingston, R. C., Winningham, J. D., & Reinisch, B. W. (1984). *F* layer ionization patches in the polar cap. *Journal of Geophysical Research*, *89*(A3), 1683–1694. https://doi.org/10.1029/JA089iA03p01683

Yee, K. (1966). Numerical solution of initial boundary value problems involving Maxwell's equations in isotropic media. *IEEE Transactions on Antennas and Propagation*, *14*(3), 302–307.

Yu, Y., & Simpson, J. J. (2011). A magnetic field-independent absorbing boundary condition for magnetized cold plasma. *IEEE Antennas and Wireless Propagation Letters*, *10*, 294–297. https://doi.org/10.1109/LAWP.2011.2139191

Zawdie, K. A., Drob, D. P., Siskind, D. E., & Coker, C. (2017). Calculating the absorption of HF radio waves in the ionosphere. *Radio Science*, *52*, 767–783. https://doi.org/10.1002/2017RS006256

Zhang, Q., Liu, R., Yang, H., Hu, H., Zhang, B., Dunlop, M., et al. (2012). SuperDARN CUTLASS Finland radar observations of high-latitude magnetic reconnections under northward interplanetary magnetic field (IMF) conditions. *SCIENCE CHINA Technological Sciences*, *55*(5), 1207–1216. https://doi.org/10.1007/s11431-012-4820-y